Effect of stacking fault energy on the restoration mechanisms and mechanical properties of friction stir welded copper alloys

Heidarzadeh, Akbar; Saeid, Tohid; Klemm, Volker; Chabok, Ali; Pei, Yutao

Published in:
Materials & design

DOI:
10.1016/j.matdes.2018.11.050

Publication date:
2019

Materials and Design 162 (2019) 185–197

Contents lists available at ScienceDirect

Materials and Design

journal homepage: www.elsevier.com/locate/matdes

Effect of stacking fault energy on the restoration mechanisms and mechanical properties of friction stir welded copper alloys

Akbar Heidarzadeh [a,*], Tohid Saeid [b], Volker Klemm [c], Ali Chabok [d], Yutao Pei [d]

[a] Department of Materials Engineering, Azarbaijan Shahid Madani University, Tabriz, Iran
[b] Faculty of Materials Engineering, Sahand University of Technology, Tabriz, Iran
[c] Institute of Materials Science, Technische Universität Bergakademie Freiberg, Germany
[d] Department of Advanced Production Engineering, Engineering and Technology Institute Groningen, University of Groningen, Nijenborgh 4, 9747AG Groningen, the Netherlands

HIGHLIGHTS

- Stacking fault energy (SFE) changes the restoration mechanisms during friction stir welding (FSW) of copper alloys.
- At higher SFE (>80 mj m^{-2}), the continuous dynamic recrystallization (CDRX) and static recovery (SRX) are active mechanisms.
- At lower SFE (<80 mj m^{-2}), in addition to CDRX, the discontinuous dynamic recrystallization (DDRX) happens during FSW.
- By decreasing SFE from 80 to 12 mj m^{-2}, the amount of DDRX increases.
- More DDRX results in higher yield strength of the joints.

GRAPHICAL ABSTRACT

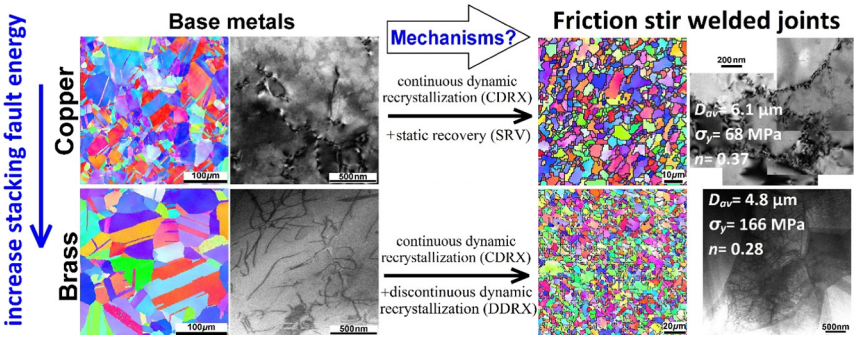

ARTICLE INFO

Article history:
Received 23 July 2018
Received in revised form 22 November 2018
Accepted 23 November 2018
Available online 24 November 2018

Keywords:
Friction stir welding
Stacking fault energy
Dynamic recrystallization,
Electron backscattered diffraction (EBSD)
Transmission electron microscopy (TEM)

ABSTRACT

Pure copper and Cu-Zn plates were friction stir welded under the same condition to evaluate the effect of stacking fault energy on the microstructural evolution and mechanical properties of the joints. For this aim, microstructure and texture of the joints were systematically characterized by electron backscattered diffraction and transmission electron microscopy. Moreover, to study the mechanical properties of the different microstructural zones of the joints, nanoindentation tests were employed. The results showed that in pure copper, continuous dynamic recrystallization was the only restoration mechanism for the formation of new grains. By adding zinc into copper, namely decreasing stacking fault energy, both continuous and discontinuous dynamic recrystallization mechanisms occurred. To this end, the effect of stacking fault energy on the restoration mechanisms has been summarized by schematic models. Moreover, the effect of the restoration mechanisms on the yield strength and strain hardening behavior of the joints has been scrutinized.

1. Introduction

Friction stir welding (FSW), a solid state welding technology, is currently used as an alternative method to fusion welding technologies for joining a wide range of metals and alloys. From a practical standpoint, FSW has a great industrial potential. In addition, from an academic viewpoint, it has attracted great interest from researchers working on this issue. Moreover, the material behavior during FSW has not been well explored. Thus, studying the microstructural aspects during FSW of metals and alloys can help to understand the basics of material behavior [1,2].

* Corresponding author.
E-mail address: ac.heydarzadeh@azaruniv.ac.ir (A. Heidarzadeh).

https://doi.org/10.1016/j.matdes.2018.11.050

Up to now, some researchers have investigated the mechanisms of grain structure formation during FSW of various metals including Al [3–14], Fe [15–19], Mg [20,21], Ti [22], and Cu based alloys [23–25]. The results of these investigations are summarized in Table 1. According to the Table 1, the restoration mechanisms of dynamic recovery (DRV), discontinuous dynamic recrystallization (DDRX), continuous dynamic recrystallization (CDRX), particle stimulated nucleation (PSN), geometric dynamic recrystallization (GDRX) and static recrystallization (SRX) can occur during FSW. The main conclusion of these investigations is that the restoration mechanisms change according to the base metal (BM) properties such as the initial microstructure (for example cold rolled or annealed) and physical properties (mainly the stacking fault energy (SFE)). In addition, FSW parameters (rotational speed, traverse speed, axial force, tool design, etc.) result in different heat input conditions, and hence various restoration mechanisms [1,2]. Therefore, to have a meaningful judgment about the effect of one parameter on the microstructural evolution during FSW, it is very necessary to keep the other parameters constant including all BM properties and process parameters.

Sakai et al. [26] have summarized the effect of SFE and processing temperature on the types of restoration mechanisms during conventional deformation processes. Accordingly, in the case of materials with low to medium SFEs (Au, Cu, Ni, Pb, austenitic Fe, and their alloys), during hot deformation ($T > 0.5T_m$), the DDRX is the dominant mechanism. However, during warm/cold deformation ($T < 0.5T_m$), the dominant mechanism is CDRX. In the case of materials with high SFEs (Al, Mg, ferritic iron, and their alloys), the dominant mechanism is CDRX during both the hot and warm/cold deformations. However, due to the complex material flow and the existence of a sharp gradient of strain, strain rate and temperature profile in FSW, the microstructural mechanisms during FSW can be much more complex in comparison with that of conventional deformation processes. To understand the material behavior during FSW, separate examination of the friction stir welded materials is necessary.

Although the above-mentioned research efforts [3–25] have disclosed the microstructural evolution during FSW of different alloys, they could hardly reveal the effect of SFE due to various used FSW parameters and different initial BM microstructures. The objective of this study was therefore to investigate the effect of SFE on the restoration mechanisms governing the microstructural evolution during FSW. For this purpose, pure copper (as a material with medium SFE among the face centered cubic (FCC) metals) and Cu-Zn alloy (as a material with low SFE among the FCC metals), which had different SFEs were friction stir welded under exactly the same condition. Orientation imaging microscopy (OIM) and transmission electron microscopy (TEM) were employed to analyze the microstructure and texture of the joints.

Table 1
Summary of different microstructural mechanisms during FSW of metals and alloys.

Base material	Mechanism	Reference
Al-Li-Cu	CDRX	[3]
7050-T651	CDRX	[4]
7050-T76	DDRX	[5]
Al-Li (AA2195)	DRV	[6]
5251-H14	CDRX	[7]
5251-O	GDRX	[7]
AA2099	GDRX and DRV	[8]
AA5083	Particle stimulated nucleation (PSN)	[8]
AA6016	DDRX and SRX	[9]
Duplex steel	In ferrite: CDRX In austenite: CDRX and SRX	[17]
Pure iron	Grain subdivision	[18]
Stainless steel (single crystal)	CDRX and DDRX	[19]
AZ31	CDRX and DDRX	[20]
Ti	DDRX	[22]
Cu	Low heat inputs: CDRX High heat inputs: DDRX	[23]
Single phase brass	CDRX and DDRX	[24]
Cu-30Zn	DDRX	[25]

2. Materials and experimental procedures

The BMs were two types of materials, including pure copper (99.99 wt% Cu with SFE of ~80 mJ m^{-2} [27]) and single phase brass with 37 wt% Zn (hereafter referred as 63B with SFE of ~12 mJ m^{-2} [27]). The plates with the same dimensions of 150 mm × 100 mm × 2 mm were friction stir welded under the equal process parameters. The rotational speed, traverse speed, and plunge depth was set constant at 400 rpm, 100 mm min^{-1}, and 0.2 mm, respectively. The FSW tool was made of H13 hot work tool steel, which was composed of a cylindrical shoulder with a diameter of 12 mm and a simple cylindrical pin with a diameter of 3 mm and a length of 1.7 mm.

The microstructure of the joints was first examined by using an optical microscopy (OM). The OM specimens were cross sectioned from the joints perpendicular to the FSW direction, and they were then prepared by mechanical polishing and etching with a solution of 50 mL HCl, 10 mL H_2O and 5 g $FeCl_3$. A Philips XL30 E-SEM field emission gun scanning electron microscope equipped with electron backscattered diffraction (EBSD) system was employed for OIM. The specimens for OIM were finalized after mechanical polishing by electropolishing for 30 s in a solution containing 250 mL H_3PO_4, 250 mL ethanol, 50 mL propanol, 500 mL distilled water, and 3 g urea at 10 V and 25 °C. TEM (JEOL JEM 2010), scanning transmission electron microscopy (STEM, Hitachi S-4800), and high-resolution transmission electron microscopy (HR-TEM, FEI Titan 300–800) were used for more clarification of the microstructural details. For TEM sample preparation of the BM and stir zone (SZ), the electrojet thinning was used with a solution of 30% H_3PO_4 and 70% distilled water at the applied potential of 80 V. For TEM characterization of the thermomechanically-affected zone (TMAZ), focused ion beam (FIB) slicing was employed to prepare TEM lamellas in a dual beam FIB/SEM microscope (Lyra, Tescan). Moreover, for investigating the mechanical properties of the different microstructural zones, nanoindentation tests were performed using MTS XP Nanoindenter equipped with a Berkovich diamond indenter. Minimum 20 indentations were conducted for each weld zones at the maximum load of 40 mN. The reverse algorithm developed by Dao et al. [28] was used to extract the local mechanical properties (yielding strength σ_y and strain hardening exponent n) from the nanoindentation data.

3. Results

The FSW joints of pure copper and 63B exhibited the same macrostructure consisting of BM, TMAZ, and SZ, as shown in Fig. 1a and b. In addition, the microstructures of the different areas from BM to SZ of the joints are illustrated in Fig. 1c–f. According to Fig. 1, BMs contained large equiaxed grains. The TMAZs in both the retreating and advancing sides of the joints were composed of elongated grains, which means that the temperature and deformation were not high enough for dynamic recrystallization (DRX). In addition, the SZs contained fine and equiaxed grains due to occurrence of DRX. Moreover, no heat-affected zone (HAZ) was observed, which is likely attributed to the low heat input condition of FSW and the high thermal conductivity of the Cu-Zn alloys [29]. In order to investigate the microstructural evolution and the restoration mechanisms during FSW, characterization of the microstructure and texture from BM to TMAZ and TMAZ to SZ is the key issue [30]. Therefore, in this study the microstructures of the BM, TMAZ, and SZ were studied in detail using EBSD and TEM that will be further discussed in the next section.

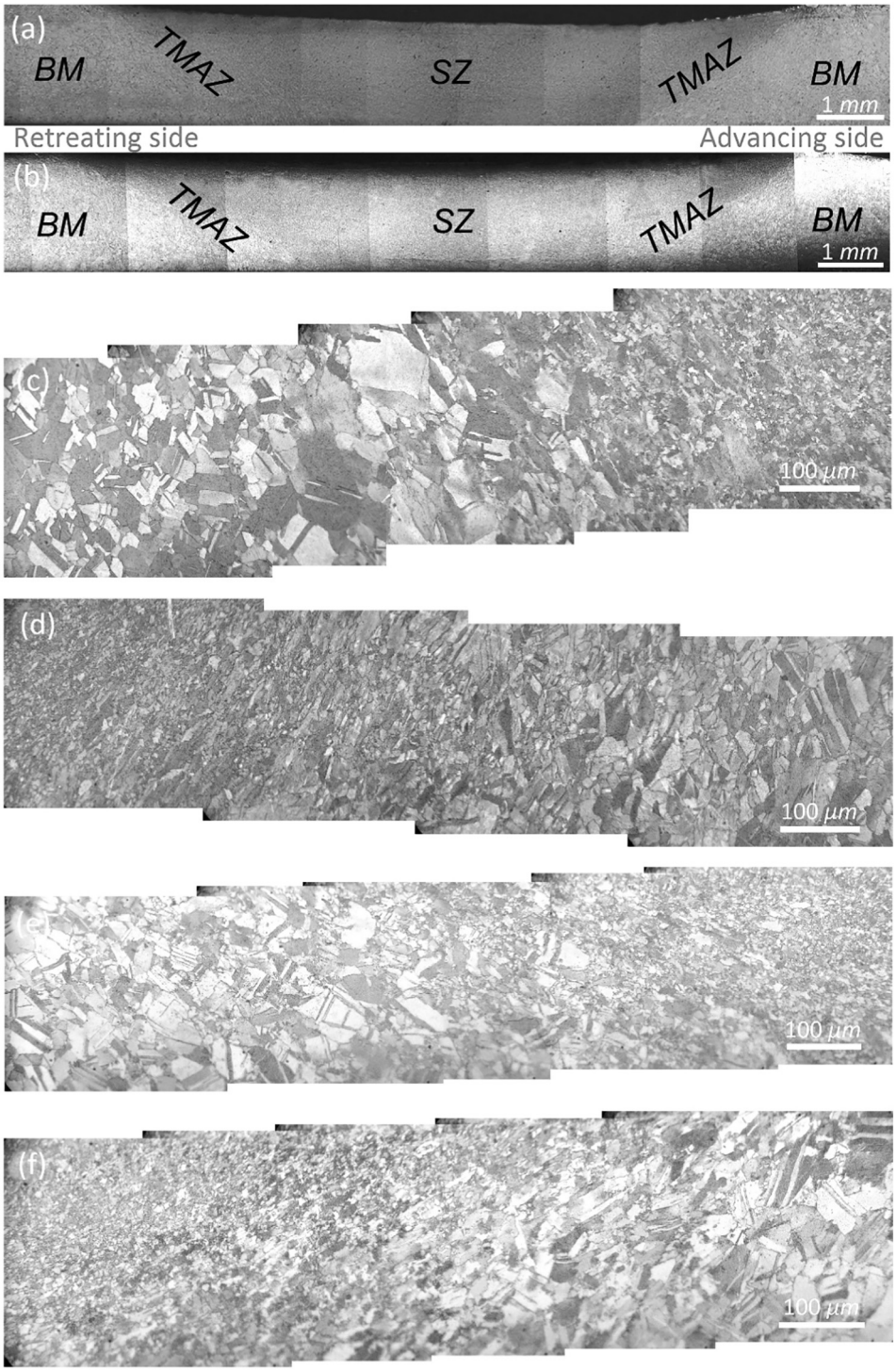

Fig. 1. The cross section macrostructure of the joints: (a) copper, and (b) 63B. The higher magnified micrographs of different regions are shown in: (c) retreating side of (a), (d) advancing side of (a), (e) retreating side of (b), and (f) advancing side of the (b).

3.1. Microstructure of different zones

3.1.1. Base metal (BM)

The inverse pole figure (IPF) map and grain boundary characterization distribution (GBCD) plot of the BMs are illustrated in Fig. 2. The BMs had an average grain size of 33 μm and 49.5 μm for the pure copper and 63B, respectively. The GBCD (Fig. 2c) shows a similar trend for the BMs. The amount of high-angle grain boundaries (HAGBs), low-angle grain boundaries (LAGBs), and twin boundaries (TBs) were 47-27-26% and 44-29-27% correspondingly for copper and 63B. This similar trend for BMs is due to their initial annealed state microstructures. The grain size of the 63B BM is larger than that of the copper BM, which may be due to higher annealing temperature for the 63B BM. Moreover, the amount of HAGBs in copper and 63B BMs is 73% and 71%, respectively, which shows that the annealing have been approximately completed. Besides, the fraction of TBs in the BMs is 23% for copper and 27% for 63B, which reveals that the grain growth has been occurred subsequent to the recovery and recrystallization during annealing.

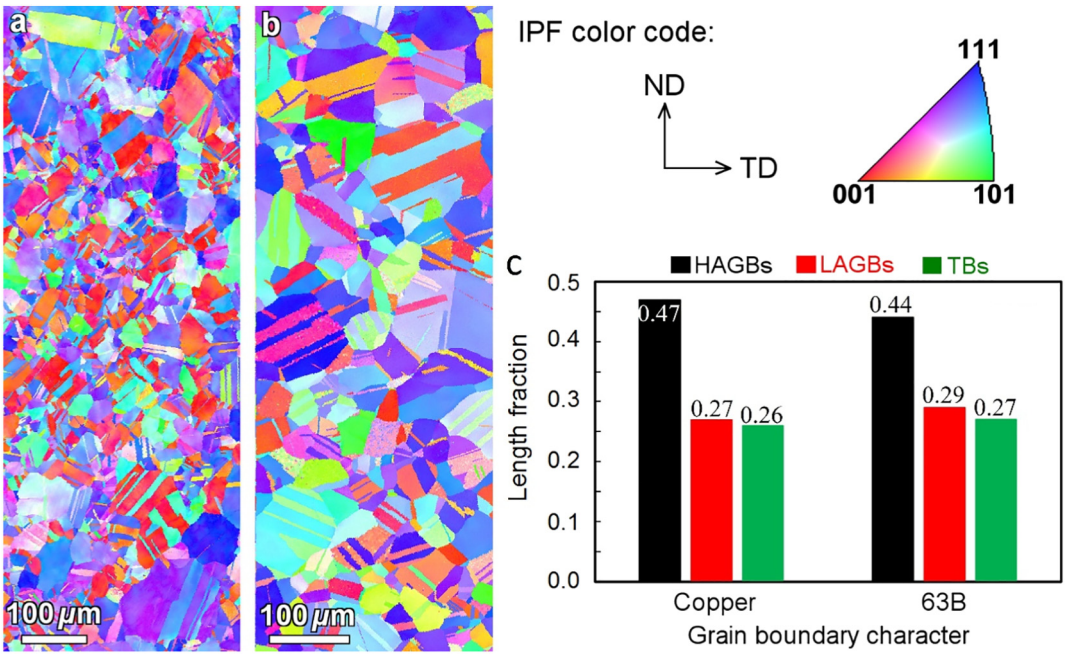

Fig. 2. (a) IPF map of pure copper BM, (b) IPF map of 63B BM, and (c) GBCD of the BMs.

3.1.2. Thermomechanically affected zone (TMAZ)

Figs. 3 and 4 illustrate the OIM analysis of the TMAZs of copper and 63B joints, respectively. In Figs. 3 and 4, the TMAZs have been divided into five regions from the point near the BM (Region 1) to the point near the SZ (Region 5) in order to elucidate the gradual transition of the microstructure from BM to SZ. From Fig. 3, the amount of LAGBs increases from BM to TMAZ Region 1, and then decreases from Region 1 to Region 5. From Fig. 4, the LAGBs in the TMAZ of 63B joint increases from R1 to R4 and then decreases to R5. By comparison between the BMs (Fig. 2) and the TMAZs (Figs. 3 and 4), the amount of TBs decreases dramatically from the BMs to the TMAZ-R1, and then increases towards the Region 5 or SZ. In this case, the lowest TB value of 2.6% belongs to the Region 2 of the copper joint. Some workers have also reported this behavior in FSW of austenitic steels [31]. In fact, TBs are Σ3 coincidence site lattice (CSL) boundaries in face centered cubic (FCC) materials which are rotated 60° about ⟨111⟩ axis. The strain applied by stirring tool leads to crystallographic rotations of these TBs from their unique orientations, and hence cause reduction of TBs from BM to Region 2 of copper, and to Region 3 of 63B. Although the initial annealing TBs have been disintegrated in TMAZs, some new Σ3 TBs have been developed in the next regions up to Region 5. Furthermore, the old GBs have been serrated in TMAZs of the joints. The other important observation is the reduction of texture intensity from Region 1 to Region 5 for 63B joint (Fig. 4) whereas in the case of copper joint there is no considerable change (Fig. 3).

3.1.3. Stir zone (SZ)

From the EBSD data of the SZs in Fig. 5, the SZ of copper joint and 63B joint possessed 50.9% and 54.7% HAGBs, 28.2% and 21.4% LAGBs, and 20.9% and 23.9% TBs, respectively. A comparison between the TMAZs and SZs reveals some important results. First, the amounts of LAGBs from the TMAZs to the SZs have decreased, whereas the values of HAGBs have increased. Second, from the TMAZs to SZs, the amounts of TBs have increased in both of the joints. In addition, there is a similarity between the GBCD of the copper and 63B SZs, however, the grain sizes of them are different. Besides the grain size, other differences, including texture, dislocation density, and dislocation structure were observed in the SZs of copper and 63B, as discussed later in the manuscript.

In order to analyze the texture components, large OIM scans were done inside the SZs of the two joints. The orientation data of (111) and (110) pole figures were extracted from the large EBSD maps. According to the method explained by Fonda [32], the as-acquired PFs were properly rotated. In this method, the texture components developed in the SZs of the joints are usually recognized by comparing them with ideal shear texture components. The ideal shear texture components are in a standard frame of reference with the shear direction (SD) pointing right and the shear plane normal (SPN) pointing up. The final rotated PFs of the SZs are illustrated in Fig. 6. From Fig. 6, for copper and 63B joints, the texture components were clear to be $A/\overline{A}$ {111}⟨110⟩ simple shear texture component. In addition, the texture strength for copper and 63B joints were 5.35 and 2.97, respectively. The main outcome of the texture results is the fact that adding Zn weakens the texture in the SZ. Moreover, in the case of 63B, from Region 5 to SZ, the texture intensity was reduced, but in the case of copper it was approximately constant (Figs. 3–4 and 6). It should be noted that the microstructures of the SZs were homogeneous, and the banded structure, which makes the texture and recrystallization process more complex, was not observed [33,34].

3.2. TEM results

The dislocation structures in BMs and SZs, and TBs in SZs are illustrated in Fig. 7. From Fig. 7a–b, the grains of BMs had a low density of dislocations, which was due to initial annealing process on the BMs. Fig. 7c–d disclose that FSW process has a significant influence on the density and structure of the dislocations, which caused the formation of high dislocation densities in the SZs. However, the dislocation structures have changed with adding Zn into copper. The SZ of copper reveals a cell dislocation structure (Fig. 7c) whereas the 63B shows tangle dislocation structures (Fig. 7d). The heat generated during FSW can cause the growth of the dynamically recrystallized grains in the welds. This can also happen after tool pass from the welding zone, statically. In addition, it is well known that the growth of SZ grains is accompanied with the formation of TBs [35]. These TBs can be produced in the forms of twin lamella and corner twin [36]. According to Fig. 7e–f, TBs were observed inside the grains of the SZs.

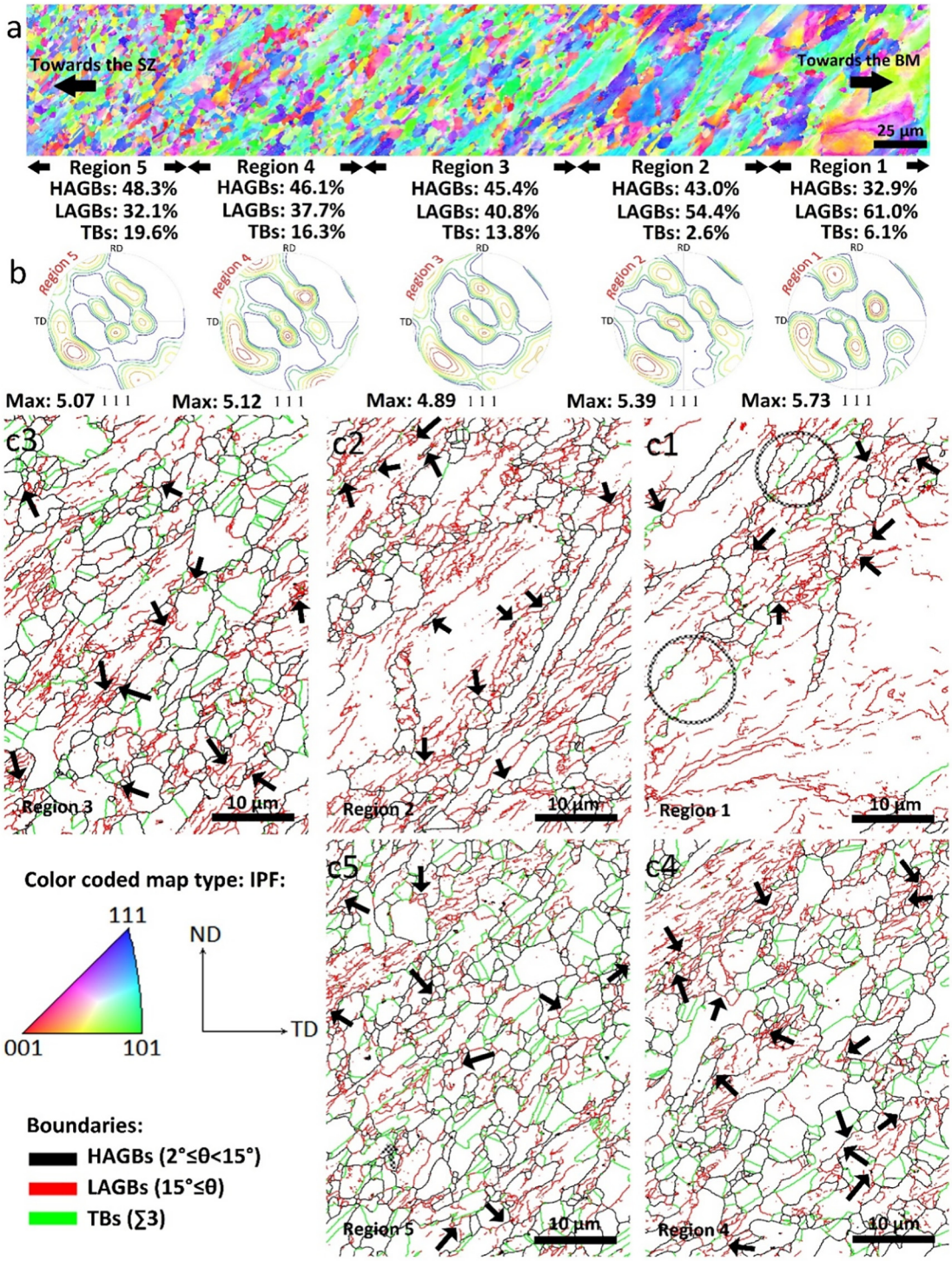

Fig. 3. (a) IPF map of the TMAZ of pure copper weld in conjunction with GBCD data for different regions, (b) as received (111) pole figures with texture strength of the different regions, (c) GB maps of the different regions. The black, red, and green lines in GB maps (c) correspond to the HAGBs ($\theta \geq 15°$), LAGBs ($2° < \theta < 15°$), and TBs boundaries, respectively. These colors are used for all the GB maps in this paper. The black arrows show the LAGBs that are partly transformed to HAGBs. The dashed circles in Region 1 (c1) refer to the initial TB, which is losing its unique orientation and is transforming to a random HAGB. (For interpretation of the references to color in this figure legend, the reader is referred to the web version of this article.)

3.3. Nano-indentation result

The nanoindentation load-displacement curves for the copper and 63B joints are illustrated in Fig. 8. In addition, the calculated n and σ_y are summarized in Table 2. The n and σ_y were equal to 0.38/55.5 MPa, 0.36/73.2 MPa, and 0.37/68.1 MPa, respectively for the BM, TMAZ and SZ of the copper joint. In the case of 63B joint, n and σ_y were measured at 0.31/111.9 MPa for BM, 0.25/217.5 MPa for TMAZ, and 0.28/166.5 MPa for SZ, respectively. The TMAZs and SZs are much stronger than the BMs, in particular that of the 63B joint. To verify the accuracy of the nanoindentation technique, the obtained results for BMs of copper and 63B brass were compared with the yield strength values using the standard tensile test. Yield strength of copper and 63B brass was measured as 58 MPa and 121 MPa, respectively, which are in good agreement with the data obtained from nanoindentation.

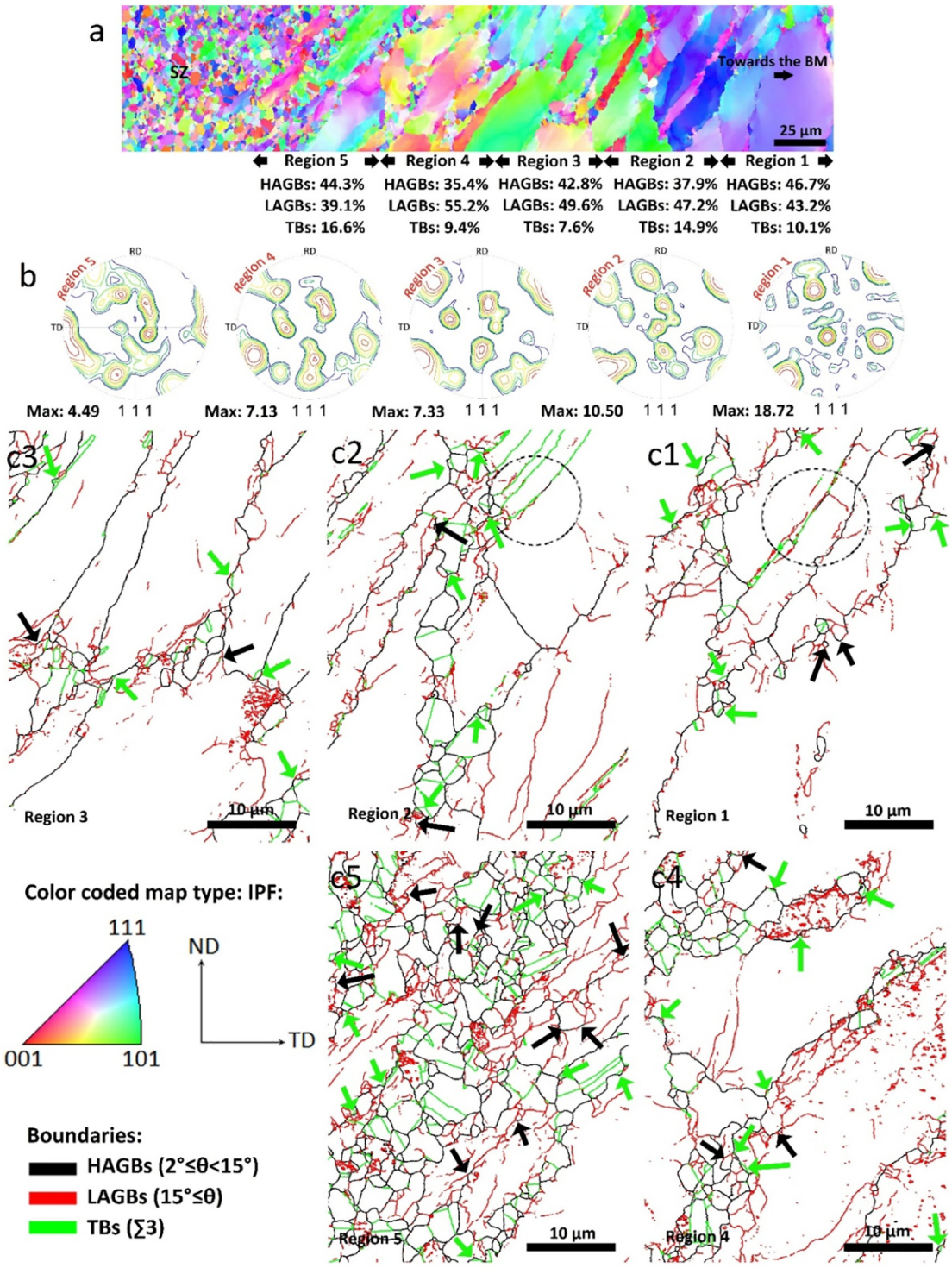

Fig. 4. (a) IPF map of the TMAZ of 63B weld in conjunction with GBCD data for different regions, (b) as received (111) pole figures with texture strength of the different regions, (c) GB maps of the different regions. The black arrows show the LAGBs transforming to HAGBs. The dashed circle in Region 1 and 2 (c1 and c2) refer to the initial TB, which are losing their unique orientation and are transforming to random HAGBs. The green arrows indicate the TBs, which are formed behind the bulged boundaries during DDRX. (For interpretation of the references to color in this figure legend, the reader is referred to the web version of this article.)

4. Discussion

In this section, possible restoration mechanisms during FSW are discussed. Finally, the effect of SFE on the grain structure formation during FSW is summarized by schematic models. In addition, the relationships between the restoration mechanisms and the mechanical properties of the joints are discussed.

4.1. Dynamic recovery (DRV) and continuous dynamic recrystallization (CDRX)

The formation of LAGBs and serrations in the primary HAGBs are the main microstructural changes during DRV [26,36]. According to the OIM analyses summarized in Figs. 3–4, the TMAZs contain a considerable fraction of LAGBs, which reveals the DRV nature of these zones. In

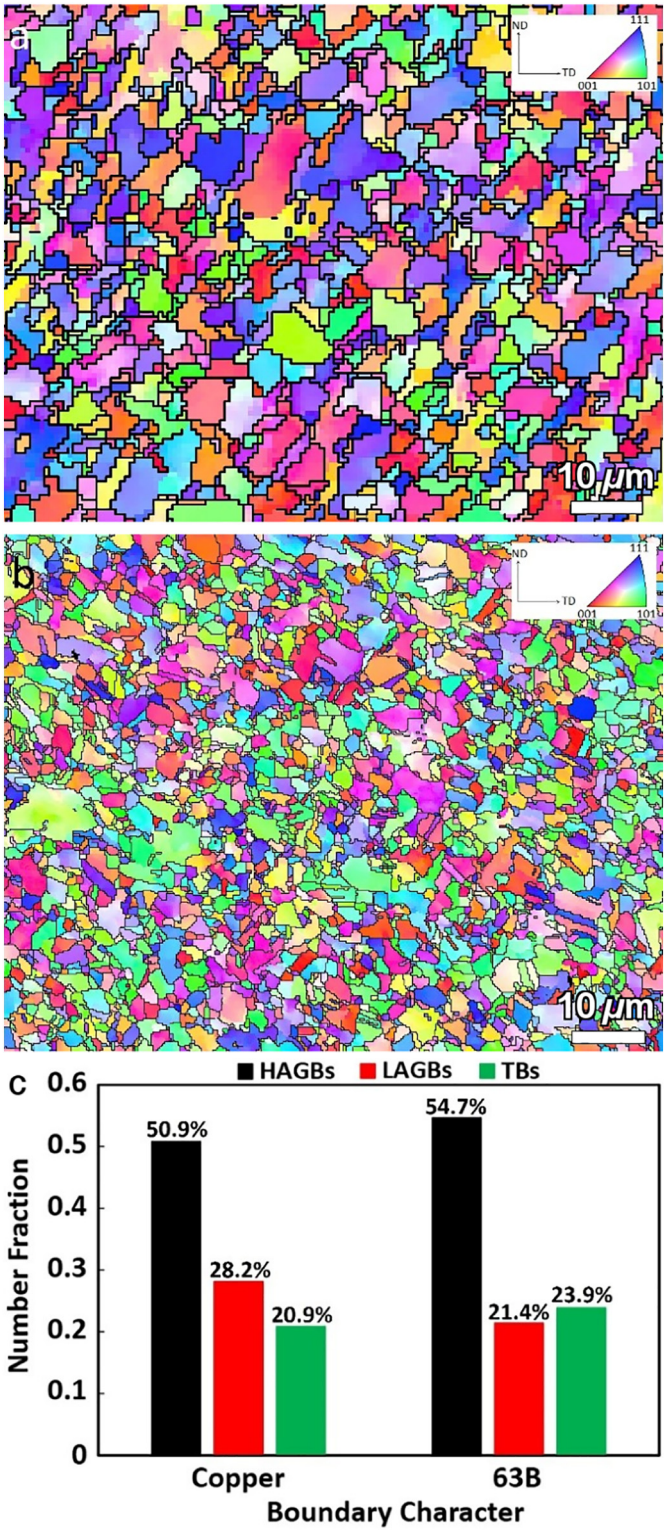

Fig. 5. IPF map of the SZ of: (a) pure copper weld and (b) 63B weld; (c) GBCD of the two SZs.

addition, the serrated GBs in the TMAZs of the joints are the other sign of the DRV. DRV can be assumed as the initial stage of the CDRX. Some researchers have reported the occurrence of CDRX during FSW of Al alloys [3,4] and steels [20]. From Fig. 3, in the TMAZ of copper joint, the amount of LAGBs increases to a maximum value of 61% in Region 1, and then from Region 2 to Region 5 it gradually decreases to 32.1%. Finally, it gets a value of 28.2% in the SZ (Fig. 5c). On the other hand,

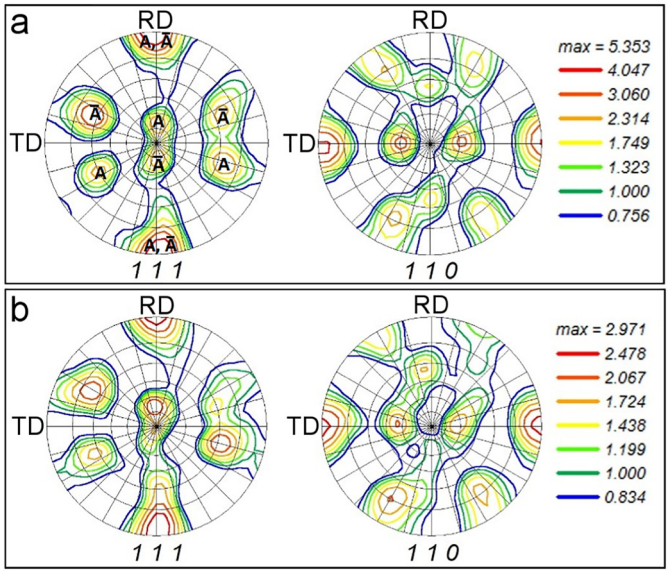

Fig. 6. The final rotated PFs of the SZs: (a) pure copper, and (b) 63B. The PFs are calculated for (111) and (110) crystallographic planes.

from Figs. 3 and 6, the HAGBs have a contrary manner, and their value increases from 32.9% in Region 1 to 48.3% in Region 5 and 50.9% in the SZ. In addition, in the different Regions of the copper TMAZ, there are some evidence of partly transformed LAGBs to HAGBs that are indicated by black arrows in Fig. 3. It is worthy to note that the conversion possibility of LAGBs to HAGBs is higher in the zones near the old GBs than inside the grains due to larger misorientation near the GBs [26]. An example of this behavior is shown in Fig. 9. Thus, CDRX is one of the governing mechanisms during grain structure formation. The approximately constant texture intensity from Region 1 to SZ of the copper (Figs. 3 and 7) confirms this claim, because CDRX typically does not change the deformation textures [29,36].

In the case of 63B joint, according to Figs. 4–5, the LAGBs to HAGBs transformations were detected similar to copper joint (black arrows in Fig. 4). However, the texture strength reduces from Region 1 to SZ of the 63B (Figs. 4 and 6). The maximum texture intensity of 18.72 in Region 1 decreases to 4.49 in region 5, and then gets a minimum value of 2.97 in SZ. The change of texture intensity means that in addition to CDRX, other mechanisms happen during FSW of 63B, which weaken the texture strength. Thus, CDRX occurs during FSW of the Cu-Zn alloys, and its amount decreases with adding Zn into copper or decreasing the SFE of the alloys.

According to the GDRX definition [36,37], the recrystallized grains along the deformation direction would have a small misorientation change in TMAZs. As shown in Fig. 10, in both cases, grains formed along the shear deformation direction in the TMAZs had large misorientation relative to each other. Therefore, GDRX unlikely operates during FSW of Cu-Zn alloys.

4.2. Discontinuous dynamic recrystallization (DDRX)

DDRX includes the nucleation and growth stages, in which the nucleation occurs by bulging of the GBs along with formation of subboundaries or TBs [26,36]. It is considered that the formation of subboundaries or TBs is dependent on the Zener-Hollomon parameter (Z). At higher and lower Z values, the formation probability of the sub-boundaries and TBs behind the bulged GBs is higher, respectively [38]. Thus, the TBs inside the grains of hot deformed metals can form during both growth stage of the recrystallized grains [35,36] and DDRX [26]. The nucleation and growth stages of the DDRX lead to necklace structures in metals with large grain sizes. Thus, the necklace structures can be a sign of DDRX, but not sufficient for judging the occurrence

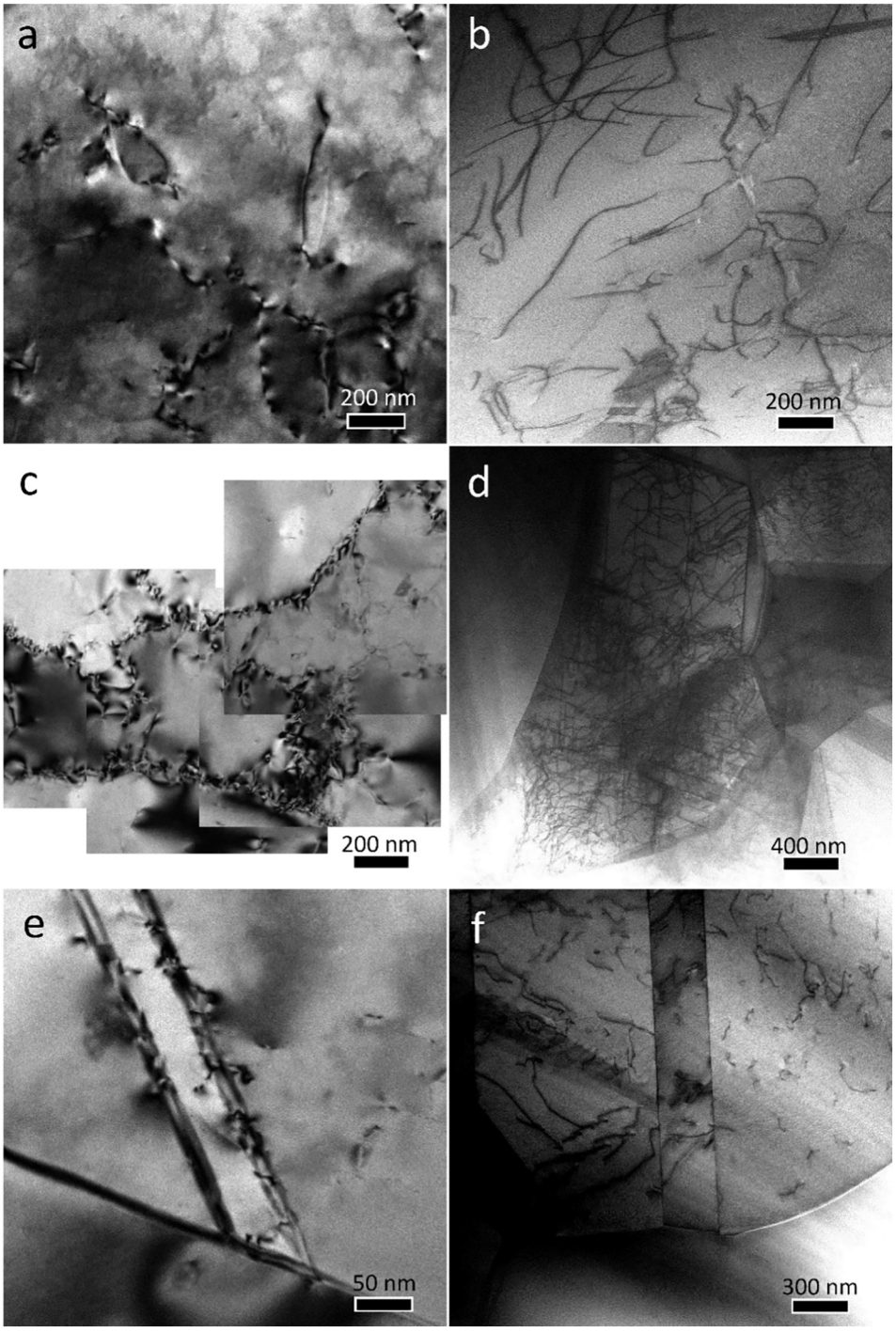

Fig. 7. STEM and TEM images of: (a) pure copper BM showing separated dislocations with low density, (b) 63B BM showing low dislocation density, (c) pure copper SZ showing dislocation cell structure, (d) 63B SZ showing dislocation tangle structure with high density, (e) copper SZ showing formation of TB, and (f) 63B SZ showing formation of TB.

of it. As already mentioned, this is because CDRX can also cause necklace structures due to the higher probability of LAGBs to HAGBs transformation near the GBs (Fig. 9). This similarity makes the texture analysis necessary in order to determine the restoration mechanisms. Unlike the CDRX, due to nucleation and growth of new grains with orientations different from those of the matrix, DDRX destroys the initial deformation texture of the matrix.

In the case of copper joint, from Figs. 2 and 3, the amount of TBs decreases from BM to 2.6% in Region 2. Due to the deformation induced by the FSW process, the unique orientation of the initial TBs of the BM changes, and hence they transform to random HAGBs. Some evidences for this TBs transformation in Region 1 are marked by dashed circles in Fig. 3. The TBs of the Region 2 are the non-transformed parts of the BM TBs. In addition, no new TBs are formed in Regions 1 and 2. However, in Regions 3–5, the amounts of TBs increase to 19.6%, and then up to 20.9% in SZ. The formation of the new TBs in Regions 3–5 is due to the growth of the CDRX grains, whereas no evidence for the formation of the DDRX TBs can be detected. This is in good agreement with constant texture intensity from Region 1 to SZ. Thus, DDRX is not taken apart in grain structure formation during FSW of pure copper.

In the case of 63B joint, the minimum amount of TBs is 7.6% in Region 3 (Fig. 4). In Regions 1–3, the initial TBs of the BM are being

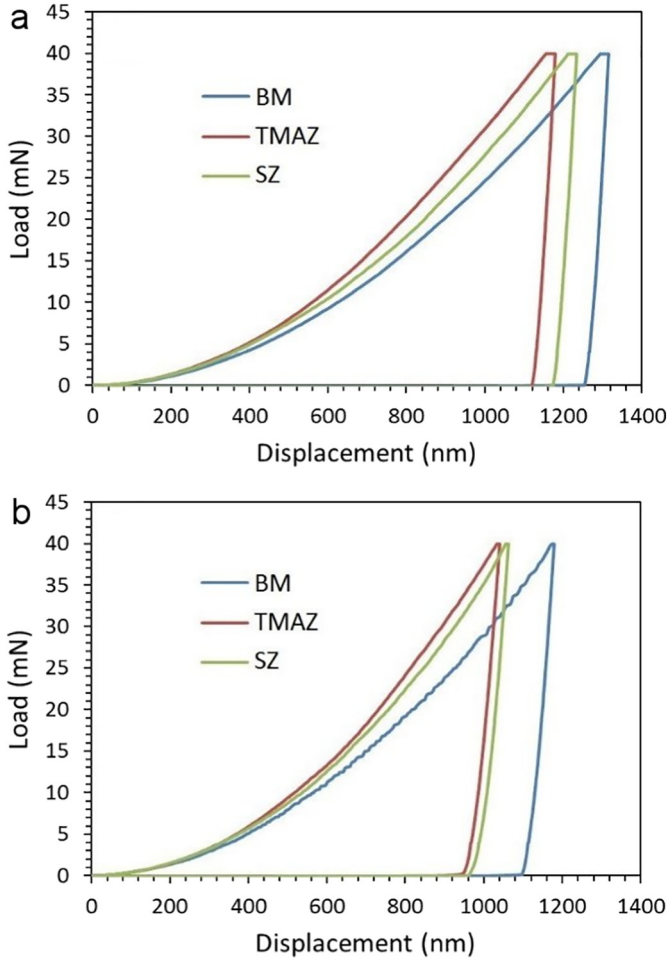

Fig. 8. The nano-indentation load-displacement curves for different zones of BM, TMAZ, and SZ of: (a) copper joint, and (b) 63B joint.

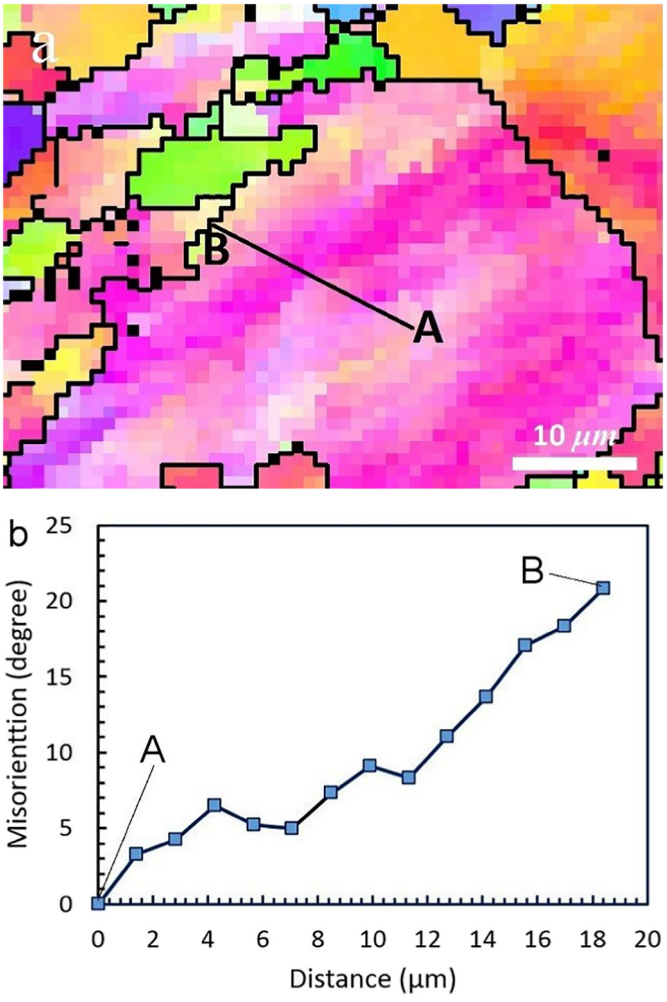

Fig. 9. (a) The IPF map of the TMAZ in pure copper joint, and (b) the accumulative misorientations along the line from point A (inside the grain) to point B (GB) indicated in (a).

destroyed (the areas indicated by dashed black circles), but simultaneously new TBs are formed shown by green arrows. This type of TBs forms behind the bulged GBs during DDRX mechanism. In Regions 4 and 5, the growth of the CDRX and DDRX grains causes formation of the new TBs. Thus, the TBs of the SZ (Figs. 5 and 7) are formed during both DDRX and growth stages.

The occurrence of DDRX in the TMAZ of 63B joint was proved using STEM, whereas no evidence was found in the case of copper. The STEM images of the 63B TMAZ with their GB schematic are illustrated in Fig. 11, which confirms the existence of DDRX by bulging and twining. From Fig. 11a and b, the GB between Grain 1 and Grain 3 has bulged towards Grain 3 (shown by blue arrows), and a TB has formed behind it, where a DDRX nuclei is also observed. The other important observation from Fig. 11a and b is GB bulging at triple points, which reveals that these sites are more suitable for nucleation compared to GBs. The triple points can be seen between Grain 1, Grain 3, and Grain 5, and between Grain 1, Grain 2, and Grain 3. The condition for GB bulging can be expressed as follows [39]:

$$\Delta E > 4k_1 {}^{\gamma_B}/_{L} \quad (1)$$

where ΔE stands for the strain energy difference per unit volume across the GB, γ_B is the GB energy per unit surface area, L represents the GB length before bulging, and K_1 is the proportionality factor, which is normally less than one under DDRX conditions. In fact, when grain boundary sliding (GBS) occurs, it is impeded by triple points, which cause larger strain gradients and more plastic accommodation, and hence larger ΔE [40].

In Fig. 11c and d, the bulging mechanism can be seen in two areas. In the first case, the GB between Grain 1 and Grain 2 has bulged from Grain 2 towards the Grain 1. This bulging mechanism has taken place along

Table 2
Summary of the microstructural and mechanical properties of the different joints. The upward arrows show the intensity of the mechanisms.

Alloy	Zone	Strain hardening exponent (n)	Yield strength (σ_y), MPa	Microstructural mechanism	Final grain size, μm	Final texture intensity
Copper	BM	0.38 ± 0.01	55.5 ± 6.2	CDRX ↑↑, SRV ↑, dislocation cells (low density)	6.12	5.35
	TMAZ	0.36 ± 0.01	73.2 ± 12.9			
	SZ	0.37 ± 0.02	68.1 ± 20.1			
63B	BM	0.31 ± 0.01	111.9 ± 11.5	CDRX↑, DDRX (bulging)↑, dislocation tangles (high density)	4.78	2.97
	TMAZ	0.25 ± 0.01	217.5 ± 18.9			
	SZ	0.28 ± 0.02	166.5 ± 35.7			

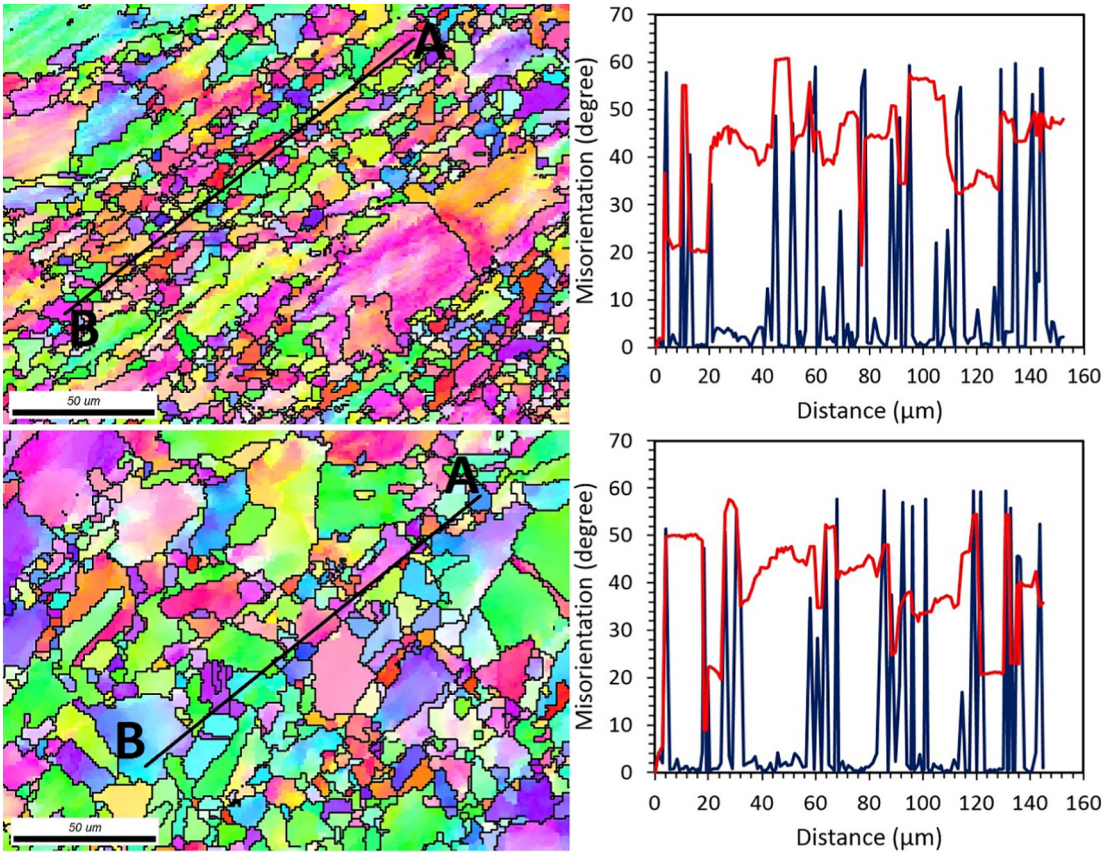

Fig. 10. EBSD IPF and phase maps of different TMAZs: (a) pure copper, and (c) 63B. Misorientation variance along the AB line shown in: b) (a), and d) (c).

the GB where ΔE was not large enough for DDRX, and hence the nucleation has not been completed. In the second case, bulging has occurred between Grain 2 and Grain 3, and the formation of TB behind it has formed the new DDRX nuclei. Indeed, the existence of two triple points on both sides of the formed DDRX nuclei has met the required ΔE. These findings are in good agreement with texture weakening from R1 to SZ of 63B (Figs. 4 and 6) that is due to occurrence of DDRX. In addition, from Fig. 6, the intensity of shear texture components decreases with adding Zn into copper (or decreasing the SFE). These results show that the DDRX is an active restoration mechanism during FSW of 63B.

4.3. Static recovery and recrystallization (SRV and SRX)

After tool passage from welding zone, static restoration mechanisms may also take place. SRV influences the substructures, for example, the dislocation structures. According to Fig. 7, the SZ of pure copper joint contains lower dislocation densities with cell structures compared to those of 63B joints with higher densities and tangle structures. Therefore, the SRV occurs during FSW of copper, but does not happen in the case of brass joint. In the case of SRX, texture analysis is the best way to determine whether SRX has occurred or not. In this regard, Cube texture component is the most common SRX texture component in FCC metals, and its existence in the SZ is the best sign of SRX [36]. According to Fig. 6, Cube texture component has not been formed during FSW, and therefore, SRX does not occur in both the cases.

4.4. Schematic models

The effect of SFE on the microstructural evolution during FSW can be summarized using the achieved results as follows. In the case of pure copper with the higher SFE, CDRX is the only mechanism governing the grain structure formation. As schematically illustrated in Fig. 12, the shear stresses caused by the rotating tool deform and elongate the grains of BM (Fig. 12b). Simultaneously, the deformed grains subdivide by DRV into new subgrains, which transform to new DRX grains by CDRX (Fig. 12c). The final CDRX grains contain dislocation cells, which is a sign of SRV. As can be seen, the schematic color of the grains from deformation step to DRX step has not been changed, which is used to show that the governing mechanisms inherit the deformation textures. By adding zinc into copper (63B brass) or decreasing the SFE, the DRX mechanism changes as schematically shown in Fig. 13. In the case of 63B, in addition to the CDRX, the DDRX takes place to form new grains by bulging mechanism at grain boundaries and triple points, which are shown by blue color areas. This mechanism does not inherit the deformation texture and leads to weaken it. In addition, the dislocations inside the DRX grains have tangle structure, which means that SRV does not occur. It can be concluded that CDRX and DDRX are competing during FSW of Cu-Zn alloys with different SFEs. At higher SFEs, the CDRX is more dominant, whereas at lower SFEs the DDRX comes to rule the grain structure formation.

To distinguish the present findings from the literature review, the following conclusions can be summarized. (1) The restoration mechanisms during FSW of copper and its alloys are not the same as the conventional deformation processes. From Ref. [26], the restoration mechanism for copper and its alloys during hot deformation processes is DDRX. However, in the present study, it is shown that both the CDRX and DDRX occur during FSW of copper and its alloys. (2) In the literature review, a wide range of FSW parameters and chemical compositions were used, and hence different mechanisms were observed. For example, in the case of aluminum alloys [3–9], several mechanisms such as DRV, CDRX, GDRX, DDRX, SPN and SRX were detected during FSW, which is due to different processing parameters and different chemical compositions. In such a combined condition, the results cannot be compared to judge about the effect of SFE. However, in the

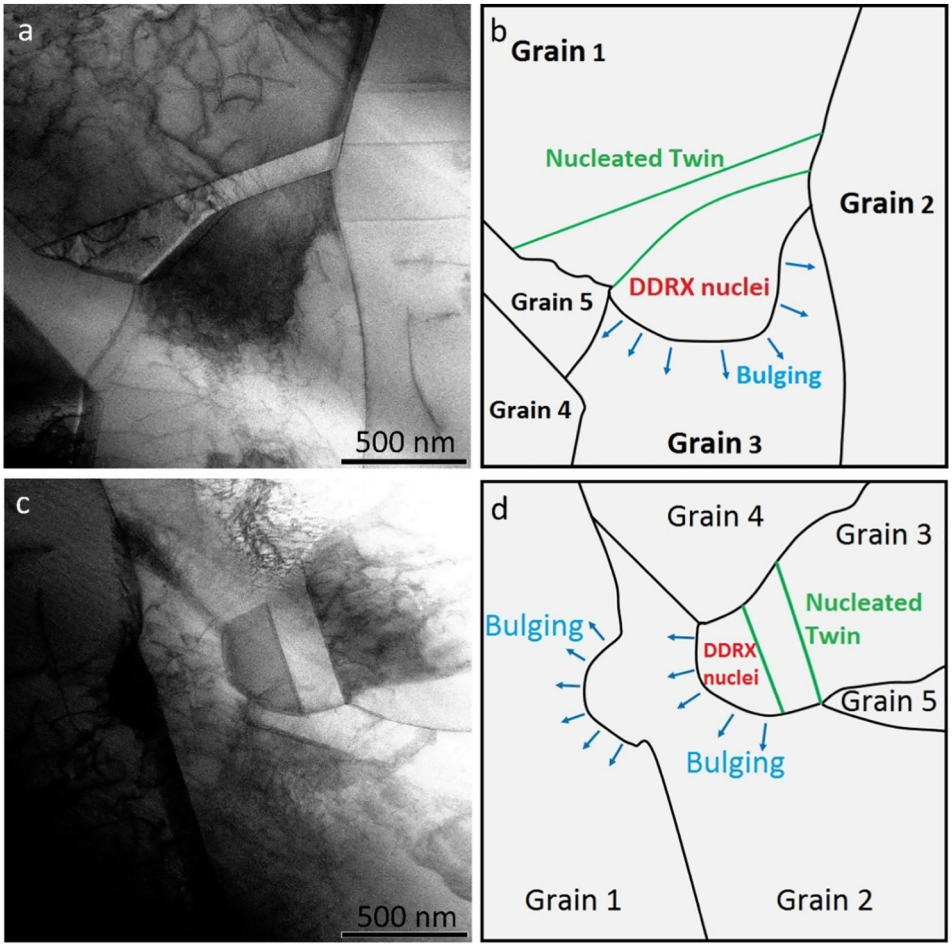

Fig. 11. STEM image of the TMAZ in 63B joint illustrating the bulging and twining during DDRX nucleation stage (a, c) and corresponding schematic illustration of GBs of (a) and (c) in (b) and (d), respectively. The HAGBs and TBs have been drawn in black and green colors. The blue arrows indicate the bulging direction of the migrating GB. (For interpretation of the references to color in this figure legend, the reader is referred to the web version of this article.)

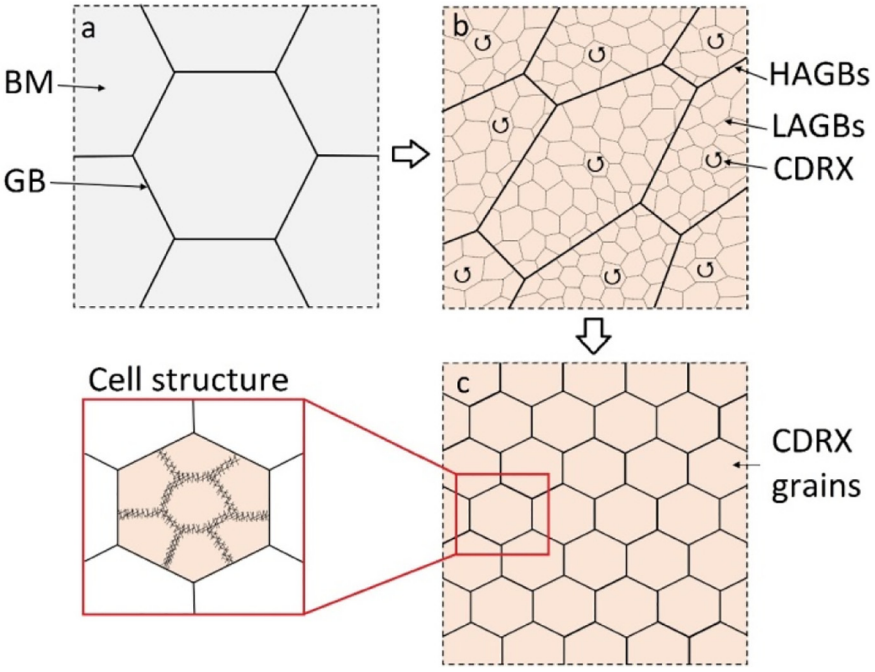

Fig. 12. Schematic illustration of microstructural evolution during FSW of pure copper.

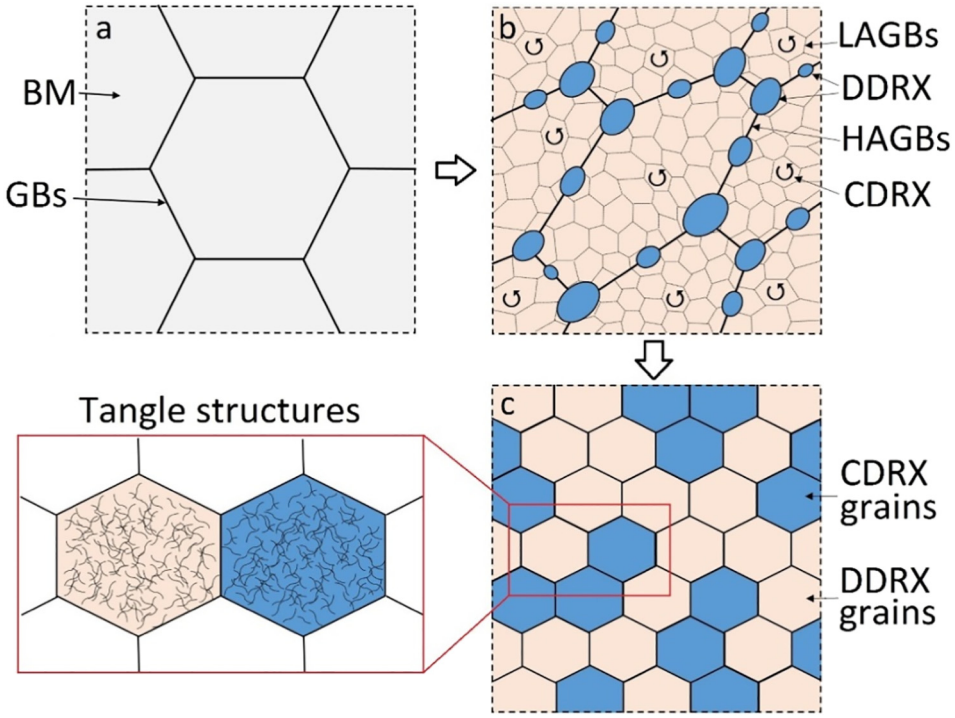

Fig. 13. Schematic illustration of microstructural evolution during FSW of 63B brass alloys.

present study, the processing parameters have been set at a constant condition, and hence the effect of chemical composition or SFE can be meaningfully identified. (3) From the literature review [23–25], the CDRX and DDRX occur during FSW of copper and its alloy. On the other hand, the FSW conditions used in Refs [23–25] are different, which causes incomparable results to verify the different mechanisms at different SFEs. In the present study, it has been shown that increasing the SFE of copper alloys leads to a change of the restoration mechanisms from CDRX to DDRX during FSW.

4.5. Relation between microstructural evolution and mechanical properties

To uncover the relation between the microstructural and mechanical properties of the joints, the value of n and σ_y, grain structure formation mechanisms, final grain size and texture intensity of the joints are summarized in Table 2. Three important points can be driven from Table 2. First, the n and σ_y of the 63B BM are lower and higher respectively than those of the pure copper. This is attributed to the solution strengthening and lower SFE of the brasses. Second, in both of the joints, the lowest n and the highest σ_y are belonged to the TMAZs. As shown in the previous sections, the TMAZs had deformed structures that contain more dislocations compared to the BMs with annealed structures and the SZs with recrystallized grains. Third, comparing the SZs of the joints reveals that by decreasing the SFE, the σ_y of the final structure increases, whereas their n values decrease. For this case, the following strengthening mechanisms are suggested. (1) By adding Zn to copper, the SFE decreases causing wider stacking faults. Consequently, the wider stacking faults reduce the mobility of the dislocations, and hence lead to higher σ_y or lower n values. (2) The solid solution strengthening causes higher σ_y and lower n of the brasses compared to the copper. (3) The SZ of 63B joint contains higher dislocation densities with tangle structures, whereas the SZ of copper joint had low dislocation density with cell structures. The higher dislocation densities and tangle structures make more obstacles against the dislocation movement, and hence the σ_y increases and n decreases. (4) The order of the joints according to their final average grain size is: copper > 63B. Therefore, the effect of grain boundary strengthening is more effective in the case of 63B.

The restoration mechanisms during FSW have a direct effect on the strengthening mechanisms of numbers 3–4. In summary, by adding Zn or lowering the SFE, the amount of DDRX increases compared to CDRX. More DDRX causes formation of dislocation tangles, higher dislocation densities, lower texture intensities, and finer grain sizes. The formation of the finer grains is attributed to the fact that DDRX produces new grains with new textures, and hence the misorientation angle between adjacent grains will be large enough to form new grains surrounded by HAGBs. On the other hand, CDRX does not produce a new texture as DDRX, and hence the material tends to form LAGBs compared to HAGBs, which produces larger grains. Thus, DDRX causes higher strength in the joints compared to the CDRX. It is worthy to note that the Zn addition in pure copper changes some other important physical properties such as melting temperature, thermal conductivity, thermal capacity, Johnson-Cook equation constants, etc., which could affect the thermomechanical history of the stirred material during the process. Elucidating these parameters can be the topic of the future investigations.

The results can be extended to various FCC materials processed by FSW at a low heat input condition. For FCC materials with SFEs higher than SFE of Cu (~80 mJ m^{-2}), the only mechanism is the CDRX. For materials with SFEs lower than that of the Cu, CDRX is replaced by DDRX, gradually. Even at very low SFEs (~12 mJ m^{-2}), CDRX happens to some extent in addition to the DDRX. Therefore, to have a completely refined DDRX structure after FSW with the best mechanical properties, another technique should be explored in addition to lowering the SFE, which is the subject of the next investigation of the authors in the field of FSW.

5. Conclusions

The effect of SFE on the restoration mechanisms during FSW Cu-Zn alloys has been investigated. At the higher SFE for pure copper, the CDRX and SRV are active mechanisms. In other words, higher SFE results in lower barrier to dislocation motion, and thus DRV and SRV can readily occur. By adding Zn to pure copper or decreasing SFE, in addition to CDRX, the DDRX happens by bulging mechanism at grain boundaries

and triple points. In 63B brass, lower SFEs inhibit DRV and cause higher dislocation densities, and hence DDRX occurs. In this case, the final dislocation structure is tangle type whereas in the case of pure copper it is cell type. The tangle structure is because of low SFE, which inhibits dislocation climb and cross slip. Therefore, in the case of brasses, CDRX and DDRX are competing during grain structure formation. Moreover, more DDRX results in higher yield strength of the joints.

Data availability

The raw/processed data required to reproduce these findings cannot be shared at this time as the data also forms part of an ongoing study.

CRediT authorship contribution statement

Akbar Heidarzadeh: Conceptualization, Data curation, Formal analysis, Investigation, Methodology, Software, Validation, Visualization, Writing - original draft, Writing - review & editing. **Tohid Saeid:** Supervision. **Volker Klemm:** Investigation, Methodology. **Ali Chabok:** Investigation, Methodology. **Yutao Pei:** Investigation, Methodology, Writing - original draft, Writing - review & editing.

References

[1] K. Gangwar, M. Ramulu, Friction stir welding of titanium alloys: a review, Mater. Des. 141 (2018) 230–255.
[2] N. Mendes, P. Neto, A. Loureiro, A.P. Moreira, Machines and control systems for friction stir welding: a review, Mater. Des. 90 (2016) 256–265.
[3] K.V. Jata, S.L. Semiatin, Continuous dynamic recrystallization during friction stir welding of high strength aluminum alloys, Scr. Mater. 43 (8) (2000) 743–749.
[4] J.Q. Su, T.W. Nelson, R. Mishra, M. Mahoney, Microstructural investigation of friction stir welded 7050-T651 aluminium, Acta Mater. 51 (3) (2003) 713–729.
[5] C.G. Rhodes, M.W. Mahoney, W.H. Bingel, M. Calabrese, Fine-grain evolution in friction-stir processed 7050 aluminum, Scr. Mater. 48 (10) (2003) 1451–1455.
[6] R.W. Fonda, J.F. Bingert, K.J. Colligan, Development of grain structure during friction stir welding, Scr. Mater. 51 (2004) 243–248.
[7] A.L. Etter, T. Baudin, N. Fredj, R. Penelle, Recrystallization mechanisms in 5251 H14 and 5251 O aluminum friction stir welds, Mater. Sci. Eng. A 445 (2007) 94–99.
[8] T.R. McNelley, S. Swaminathan, J.Q. Su, Recrystallization mechanisms during friction stir welding/processing of aluminum alloys, Scr. Mater. 58 (2008) 349–354.
[9] U.F.H.R. Suhuddin, S. Mironov, Y.S. Sato, H. Kokawa, Grain structure and texture evolution during friction stir welding of thin 6016 aluminum alloy sheets, Mater. Sci. Eng. A 527 (2010) 1962–1969.
[10] X.C. Liu, Y.F. Sun, H. Fujii, Clarification of microstructure evolution of aluminum during friction stir welding using liquid CO_2 rapid cooling, Mater. Des. 129 (2017) 151–163.
[11] M. Reimann, J. Goebel, J.F. dos Santos, Microstructure and mechanical properties of keyhole repair welds in AA 7075-T651 using refill friction stir spot welding, Mater. Des. 132 (2017) 283–294.
[12] N. Guo, Y. Fu, Y. Wang, Q. Meng, Y. Zhu, Microstructure and mechanical properties in friction stir welded 5A06 aluminum alloy thick plate, Mater. Des. 113 (2017) 273–283.
[13] H. Sidhar, N.Y. Martinez, R.S. Mishra, J. Silvanus, Friction stir welding of Al–Mg–Li 1424 alloy, Mater. Des. 106 (2016) 146–152.
[14] M. Esmaily, N. Mortazavi, W. Osikowicz, H. Hindsefelt, J.E. Svensson, M. Halvarsson, et al., Bobbin and conventional friction stir welding of thick extruded AA6005-T6 profiles, Mater. Des. 108 (2016) 114–125.
[15] F.C. Liu, T.W. Nelson, In-situ grain structure and texture evolution during friction stir welding of austenite stainless steel, Mater. Des. 115 (2017) 467–478.
[16] H. Li, S. Yang, S. Zhang, B. Zhang, Z. Jiang, H. Feng, et al., Microstructure evolution and mechanical properties of friction stir welding super-austenitic stainless steel S32654, Mater. Des. 118 (2017) 207–217.
[17] T. Saeid, A. Abdollah-zadeh, T. Shibayanagi, K. Ikeuchi, H. Assadi, On the formation of grain structure during friction stir welding of duplex stainless steel, Mater. Sci. Eng. A 527 (2010) 6484–6488.
[18] S. Mironov, Y.S. Sato, H. Kokawa, Microstructural evolution during friction stir-processing of pure iron, Acta Mater. 56 (11) (2008) 2602–2614.
[19] J. Jeon, S. Mironov, Y. Sato, H. Kokawa, S. Park, S. Hirano, Grain structure development during friction stir welding of single-crystal austenitic stainless steel, Metall. Mater. Trans. A 44 (7) (2013) 3157–3166.
[20] S. Mironov, T. Onuma, Y.S. Sato, H. Kokawa, Microstructure evolution during friction-stir welding of AZ31 magnesium alloy, Acta Mater. 100 (2015) 301–312.
[21] J. Han, J. Chen, L. Peng, S. Tan, Y. Wu, F. Zheng, et al., Microstructure, texture and mechanical properties of friction stir processed Mg-14Gd alloys, Mater. Des. 130 (2017) 90–102.
[22] S. Mironov, Y. Zhang, Y.S. Sato, H. Kokawa, Development of grain structure in β-phase field during friction stir welding of Ti–6Al–4V alloy, Scr. Mater. 59 (1) (2008) 27–30.
[23] S. Mironov, K. Inagaki, Y.S. Sato, H. Kokawa, Microstructural evolution of pure copper during friction-stir welding, Philos. Mag. 95 (4) (2015) 367–381.
[24] A. Heidarzadeh, T. Saeid, V. Klemm, Microstructure, texture, and mechanical properties of friction stir welded commercial brass alloy, Mater. Charact. 119 (2016) 84–91.
[25] X. Liu, Y. Sun, T. Nagira, K. Ushioda, H. Fujii, Microstructure evolution of Cu–30Zn during friction stir welding, J. Mater. Sci. 53 (2018) 10423–10441.
[26] T. Sakai, A. Belyakov, R. Kaibyshev, H. Miura, J.J. Jonas, Dynamic and post-dynamic recrystallization under hot, cold and severe plastic deformation conditions, Prog. Mater. Sci. 60 (2014) 130–207.
[27] M.F. Denanot, J.P. Villain, The stacking fault energy in Cu-Al-Zn alloys, Phys. Status Solidi A 8 (1971) K125–K127.
[28] M. Dao, N. Chollacoop, K.J. Van Vliet, T.A. Venkatesh, S. Suresh, Computational modeling of the forward and reverse problems in instrumented sharp indentation, Acta Mater. 49 (2001) 3899–3918.
[29] A. Heidarzadeh, T. Saeid, A comparative study of microstructure and mechanical properties between friction stir welded single and double phase brass alloys, Mater. Sci. Eng. A 649 (2016) 349–358.
[30] A. Heidarzadeh, K. Kazemi-Choobi, H. Hanifian, P. Asadi, 3 - microstructural evolution, in: M.K.B. Givi, P. Asadi (Eds.), Advances in Friction-stir Welding and Processing, Woodhead Publishing 2014, pp. 65–140.
[31] S. Mironov, Y.S. Sato, H. Kokawa, H. Inoue, S. Tsuge, Structural response of superaustenitic stainless steel to friction stir welding, Acta Mater. 59 (14) (2011) 5472–5481.
[32] R.W. Fonda, K.E. Knipling, D.J. Rowenhorst, EBSD analysis of friction stir weld textures, JOM 66 (1) (2014) 149–155.
[33] D. Texier, Y. Zedan, T. Amoros, E. Feulvarch, J.C. Stinville, P. Bocher, Near-surface mechanical heterogeneities in a dissimilar aluminum alloys friction stir welded joint, Mater. Des. 108 (2016) 217–229.
[34] M. Dhondt, I. Aubert, N. Saintier, J.M. Olive, Mechanical behavior of periodical microstructure induced by friction stir welding on Al–Cu–Li 2050 alloy, Mater. Sci. Eng. A 644 (2015) 69–75.
[35] P. Xue, G.M. Xie, B.L. Xiao, Z.Y. Ma, L. Geng, Effect of heat input conditions on microstructure and mechanical properties of friction-stir-welded pure copper, Metall. Mater. Trans. A 41 (8) (2010) 2010–2021.
[36] F.J. Humphreys, M. Hatherly, Chapter 13 - hot deformation and dynamic restoration, in: F.J.H. Hatherly (Ed.), Recrystallization and Related Annealing Phenomena, Second editionElsevier, Oxford 2004, p. 415-V.
[37] P.B. Prangnell, C.P. Heason, Grain structure formation during friction stir welding observed by the 'stop action technique', Acta Mater. 53 (11) (2005) 3179–3192.
[38] M. Ghosh, K. Kumar, R.S. Mishra, Analysis of microstructural evolution during friction stir welding of ultrahigh-strength steel, Scr. Mater. 63 (8) (2010) 851–854.
[39] H. Miura, H. Aoyama, T. Sakai, Effect of grain-boundary misorientation on dynamic recrystallization of Cu-Si bicrystals, J. Jpn. Inst. Metals 58 (3) (1994) 267–275.
[40] H. Miura, T. Sakai, S. Andiarwanto, J.J. Jonas, Nucleation of dynamic recrystallization at triple junctions in polycrystalline copper, Philos. Mag. 85 (23) (2005) 2653–2669.